


Geometry-induced rectification of looped oscillatory flows

Ruy Ibanez, Aditya Raghunandan, and Douglas H. Kelley 

Department of Mechanical Engineering, University of Rochester, New York 14627, USA



(Received 10 May 2023; accepted 18 October 2023; published 9 November 2023)

In this study, we leverage geometry-induced asymmetries to rectify oscillatory flows and induce net directional transport of fluid in a looped network. We demonstrate this valveless rectification phenomenon in an experimental apparatus that consists of an acrylic flow chamber with a deformable wall connected to a syringe pump via a T-junction. Here, oscillatory flows were forced by the syringe pump. We found that the asymmetries that existed in the geometric configuration of the looped channel could be exploited to generate net directional flow and that this geometric configuration is key in determining the directionality. By varying the pumping parameters in the system, we determined a relationship between the frequency and stroke length of the forcing syringe pump and the resulting directional flow in the loop. Using an analytical model and flow computations, we posit how asymmetric flow separation occurring at the T-junction could explain the observed flows.

DOI: [10.1103/PhysRevFluids.8.113101](https://doi.org/10.1103/PhysRevFluids.8.113101)

I. INTRODUCTION

Rectification of oscillatory fluid motion is a form of pumping that occurs in both physiological and laboratory flows across length scales [1]. Conventionally, rectification is achieved by the use of moving components such as valves. For example, the oscillatory flow of blood or lymphatic fluid in the body is rectified by biological valves that open and close to regulate and direct the net unidirectional transport of fluid across a large connected network of vessels [2–7]. Valveless rectification is also possible, and is primarily achieved by exploiting the kinematic irreversibility of inertia-dominated flows at moderate to high Reynolds numbers (Re) [8]. Examples of such applications include static geometries such as fluidic diodes developed by Tesla [9], and moving geometries such as converging-diverging conduits [10], sawtoothed corrugations [11], and others [12–14]. Applications exploiting the fluid’s viscoelastic properties to rectify flow have also been developed [15].

In this study, we present a simpler form of rectification where we leverage the geometric asymmetries of looped fluidic networks induced by common pathway geometries such as T-junctions. Using experimental measurements and flow computations, we demonstrate rectification of oscillatory flows and directional transport of fluid in a closed loop that includes a T-junction at low-to-moderate Re . We were motivated to study this mechanism in order to gain a better understanding of oscillatory fluid flows in branched physiological networks that have an apparent net direction of fluid transport but with a yet unknown rectification mechanism, such as the recently discovered transport of fluid in the brain via the “glymphatic” circulation system [16]. There, the oscillatory motion of cerebrospinal fluid (CSF) in perivascular spaces, induced by the pulsation of the arterial walls, is rectified and converted into net directional transport along a complex branched network. For this study, we focused on the fact that channel structures in the pathways of the glymphatic system have numerous bifurcations [17], and measurements of the glymphatic system show that the flow possesses an oscillatory component combined with net directional transport [18–20].

The experimental system we devised consists of a syringe pump connected to a channel with a deformable wall in a closed loop via a T-junction. These components were intended to capture

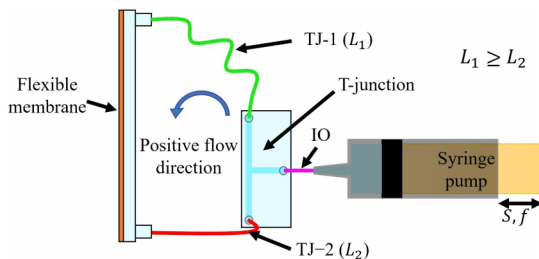


FIG. 1. Schematic of the experimental apparatus. A custom syringe pump displaces fluid in and out of the looped section of the system via a T-junction. A pressure relief membrane allows the incompressible fluid to be displaced as the syringe injects fluid. The sketch indicates the direction of flow in the loop which we define to be positive.

the previously stated key features: The syringe pump (akin to the heart) produced the oscillatory flow, the channel with a movable wall represents the typical perivascular compartment, while the T-junction is intended to capture the effects of the bifurcating network structure. Using this setup, we demonstrate that simple oscillatory flows induced in the network can be rectified to produce net flow at low to moderate Re . We also show that the direction and speed of flows can be controlled by simple geometric manipulation of network connections.

II. METHODS

A. Device description

Figure 1 shows the experimental apparatus. The bespoke syringe pump assembly was built using a linear translational stage, consisting of linear rails, that is mounted on a threaded stainless-steel shaft coupled to a linear stepper motor. A 100 mL plastic syringe was mounted to the stage, with the plunger connected to the linear rail block. The movement of the stage drives fluid in and out of the syringe. This linear motion of the stage is achieved via the rotation of a stepper motor that is coupled to the shaft on which the stage is mounted. Stepper motor rotation was achieved with the help of a motor controller (Pololu AMIS-30543) connected to a microcontroller chip (Arduino MEGA 2560). The native Arduino software was used to calibrate the rotation speeds, adjust the induced linear displacement, and tune the required experimental parameters. The outlet of the syringe is connected to the central arm of a manufactured T-junction connected to Tygon tubing (4.76 mm inner diameter, 6.35 mm outer diameter, McMaster-Carr: 6516T17). Thus, with respect to the T-junction, the syringe pump injected fluid symmetrically, i.e., the distance from the end of the two outlet arms to the syringe is equal. The T-junction was constructed by stacking layers of acrylic sheets that are laser cut and sealed together by placing rubber gaskets between layers. The acrylic sheets and rubber gaskets are clamped and sealed by through-bolts located around the edge of the sheets. The other two arms of the T-junction were connected, via the same tubing, to the two ends of a manufactured acrylic rectangular channel with cross-sectional dimensions $8.26 \text{ mm} \times 3.18 \text{ mm}$, and 95.25 mm in length. The channel was built using stacked laser-cut sheets of acrylic in a similar fashion to the T-junction. To allow for pressure relief when the fluid in the syringe was compressed, the bottom surface of the channel was made using a thin 0.15 mm rubber sheet (McMaster-Carr: 85995K12) which is allowed to deflect.

B. Inducing fluid motion

Oscillatory fluid motion was induced by the back-and-forth motion of the bespoke syringe pump. The range of experimental parameters was varied by modifying the stroke length (linear displacement) of the pump S , the frequency of oscillation f , and the lengths of the tubes connecting

the T-junction to the acrylic channel. We will refer to the two tubes in the loop as T-1 and T-2, with lengths L_1 and L_2 , respectively. Note that for all cases we discuss, T-1 was at least as long as T-2, i.e., $L_1 \geq L_2$. The total length of the tube, $L_T = L_1 + L_2$, was kept constant. The length of the inlet and outlet tube, IO, which connects the syringe and T-junction, was also kept constant. For the configuration shown in Fig. 1, the system can be considered to be symmetric with respect to the syringe and membrane when $L_1 = L_2$ and asymmetric when $L_1 > L_2$.

One can think of the syringe motion as a velocity boundary condition on the looped system. As the syringe changes in volume, fluid must be pushed at an average velocity dictated by the change in volume. Thus, given that diameter of the syringe is 3.8 cm and the tubing is 4.7 mm in diameter, $\bar{u} = A_{\text{syringe}}/A_{\text{tube}}Sf = 15.9Sf$, where \bar{u} , A_{syringe} , and A_{tube} are the average velocity of the channel IO, the cross-sectional area of the syringe, and the cross-sectional area of IO, respectively.

C. Data acquisition

To visualize and measure flow, the apparatus was filled with an aqueous suspension of fluorescent microspheres (Cospheric) of diameter 100 μm and density of 1 g/cm^3 , suspended in deionized (DI) water. Once flow was initiated, the areas of interest were illuminated using an LED lamp (McMaster-Carr). The flow and motion of the suspended microspheres in the apparatus were recorded at ranges of 30 to 200 frames per second using a high-speed camera (Emergent 4000M). The recorded images had pixel dimensions 2048 \times 300 for measurements at the tubing section, and 1000 \times 800 for measurements at the T-junction. To visualize and record videos of the flow patterns at the T-junction, we also used a rheoscopic fluid produced from shaving cream following the methods listed in Ref. [21].

D. Data processing

Measurements in the form of videos were captured at sections of T-1 or at the T-junction. The recorded movies were processed using an in-house MATLAB-based particle tracking velocimetry (PTV) software suite [22]. PTV provided us with measured paths and instantaneous velocities of individual particles. When we varied the syringe pump parameters S and f , the tubing lengths L_1 and L_2 , and the interloop connections (further discussed in Sec. III), we used particle path measurements at a section of T-1 to determine if a net velocity was present. Since there were no outlets for fluid, we assumed that the time-averaged net flow at T-1 would be equal and opposite at T-2.

E. Numerical simulations

We performed numerical steady-state simulations using the commercial software ANSYS Fluent. We modeled and analyzed a series of two-dimensional T-junctions, as shown in Fig. 9. We used two different sets of boundary conditions: In the first case, we set the pressure to zero at two outlets and specified the flow rate at one inlet. In the second case, we specified the flow rates at the outlets and changed the inlet condition to zero pressure. We used the laminar flow model for a steady-state case with a mesh consisting of 10^5 quadratic elements. The numerical models were checked for convergence and mesh quality by progressively decreasing the mesh size until convergence in the solutions was achieved, where vorticity and velocity results showed variations of less than 1% over the domain.

III. RESULTS

A. Measurements at the loop

To determine if a net directional flow was produced, we measured particle paths by recording and processing videos (as discussed in Sec. II) captured in a 7-cm-long section of T-1. Representative particle paths are shown in Fig. 2. We observed that the particles oscillated regularly, matching the

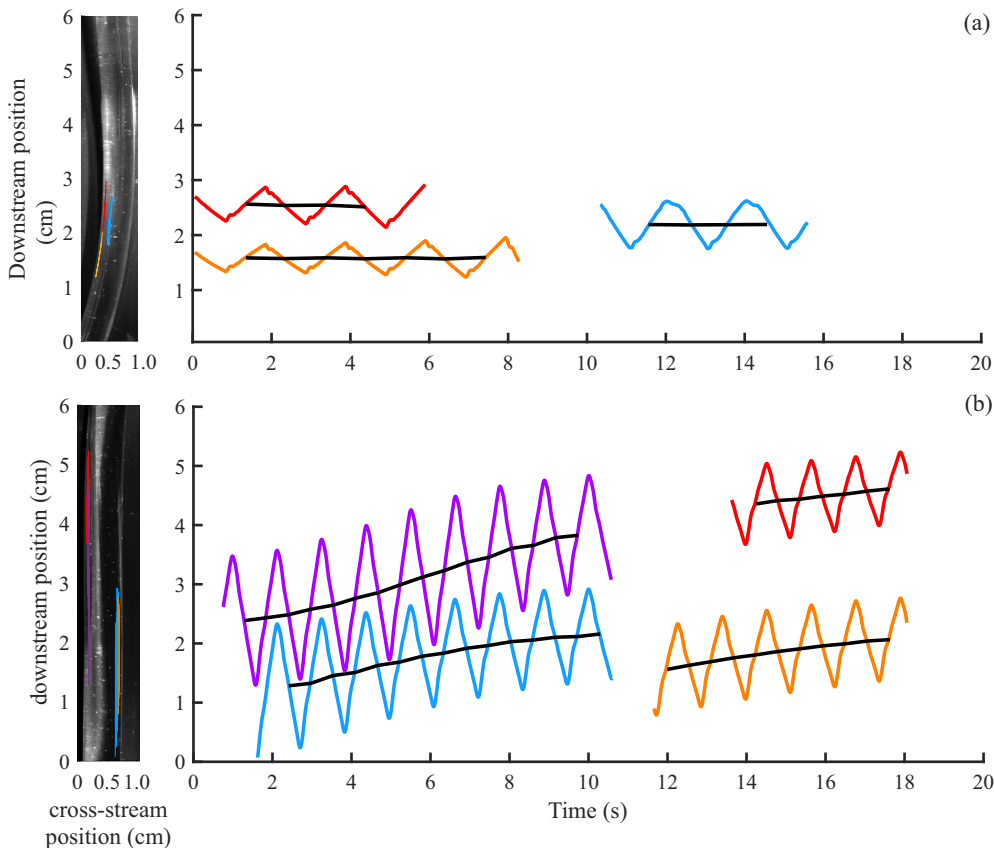


FIG. 2. Downstream particle positions in a section of T-1, with each particle path colored differently. The left image shows the tube section corresponding to the positions plotted on the plot to the right. The black lines delineate the average position of the particle over time. (a) With parameters $f = 0.5$ Hz, $S = 2.0$ mm, $\gamma = 1$, $L_t = 80$ cm, particles oscillate without any net velocity. (b) With parameters $f = 1$ Hz, $S = 2.0$ mm, $\gamma = 4$, $L_t = 80$ cm, particles and the surrounding fluid have a net velocity as they drift away from the visible area.

frequency of the syringe pump. During our measurements, it was evident that there was often a nonperiodic, directional component to the particle's motion.

To quantify this nonperiodic motion of each particle, we first excluded particle paths shorter than three periods, i.e., duration $3/f$. Then, we applied a five-frame moving average to reduce the noise level in the measurements. That allowed us to precisely find the times at which each particle was momentarily at rest: An oscillating particle was at rest twice during each oscillation cycle. To determine the net displacement of each particle, we integrated its instantaneous velocity measured by particle tracking over an interval spanning an even number of resting moments. Dividing the net displacement by the duration of the interval yielded the net velocity of the directional, nonperiodic motion of each particle, which can be seen in Figs. 2(a) and 2(b).

Figure 2 also shows that oscillating particles experienced a small net displacement over time if and only if the tubing lengths were unequal. For brevity, we denote the ratio of their lengths $\gamma = L_1/L_2$. When $\gamma = 3$, net displacement is evident when observing that the values of minima (or maxima) in the downstream position increase with time. For $\gamma = 1$, particles oscillate without experiencing net displacement (extreme values of downstream position remain the same).

Having identified that γ affected particle displacement, we then performed a series of experiments where we varied the S , f , and γ to determine critical parameters affecting net flow. Figure 3

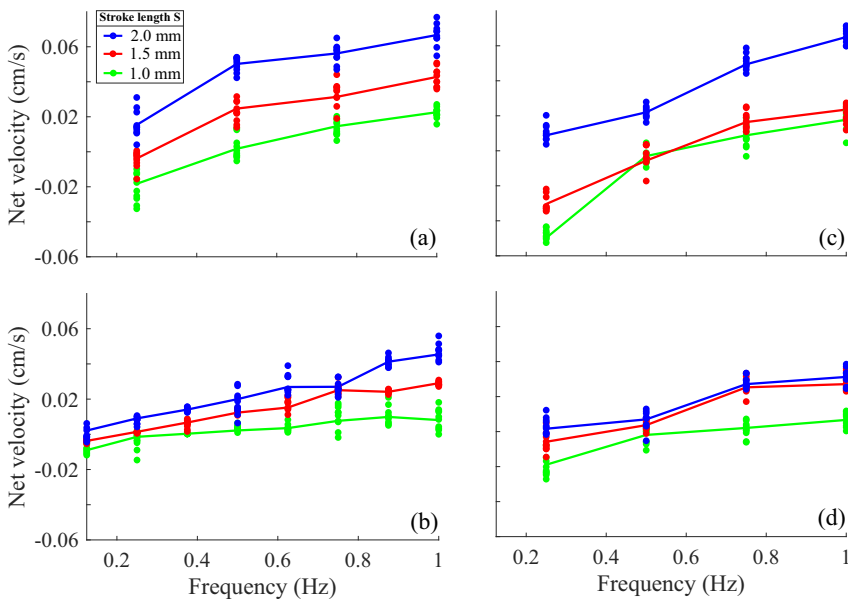


FIG. 3. Experimentally measured net velocities in a segment of T-1, for a diverse set of parameters. $L_t = 80$ cm for all measurements shown, but γ varies: (a) $\gamma = 2$, (b) $\gamma = 4$, (c) $\gamma = 3$, and (d) $\gamma = 7$. We observed no strong effect on net velocity due to γ . Stroke length S and frequency f had the strongest effects on the net velocity, and at the lower values we found that the net velocity tended to reverse.

shows the measured net velocities for different combinations of parameters. We find that for most parameter regimes of interest, the direction of net flow follows a path that begins at T-1, leads into the channel with the pressure relief membrane, and then out via T-2. In other words, in Fig. 1 the flow would follow a counterclockwise direction around the loop.

For any given γ , increasing the frequency resulted in faster flows with a monotonic increase in net velocities around the loop, with flow primarily in the counterclockwise direction. However, at low frequencies (0.1–0.3 Hz), we observed a reversal in flow (i.e., fluid would flow clockwise in the loop) indicated by the negative magnitudes of net velocity in Fig. 3. This reversal of flow was most apparent for the shortest stroke length of $S = 1$ mm.

For a given γ , increasing the stroke length also induced a monotonic increase in the net flow velocities: the larger the stroke length, the faster the induced flow magnitudes as more fluid was displaced in each oscillation. By increasing γ , we were able to induce faster flows, reaching a maximum speed of 0.6 mm/s measured at $\gamma = 7$ and $f = 1$ Hz.

The efficiency of producing net transport from an oscillatory flow in the system was estimated in a manner similar to that described in Nguyen *et al.* [14]. We defined the efficiency E of producing a net flow (rectification) as $E = u_{\text{net}} A_1^{-1} f^{-1} / 2$, where A_1 is the measured amplitude of oscillation at T-1. As shown in Fig. 4, the highest efficiencies were found at lower frequencies, accompanied by a negative net flow direction. With an increase in frequency, efficiency decreased until the net flow became positive. At this point the efficiency again increased, but with largely diminishing returns.

To explain the observed directional flows, we first hypothesized that our experimental setup might be a form of an impedance pump [23], where directionality was induced by the mismatch in the stiffness between the tubing, flexible membrane, and the rigid T-junction [23,24]. However, when we tested tubing with different Shore hardness of 65A, 85A, and 95A durometer, we observed no change in the directionality of induced flows, nor in the magnitude of measured flow velocities. Those observations ruled out material mismatch-related impedance pumping as the driving mechanism.

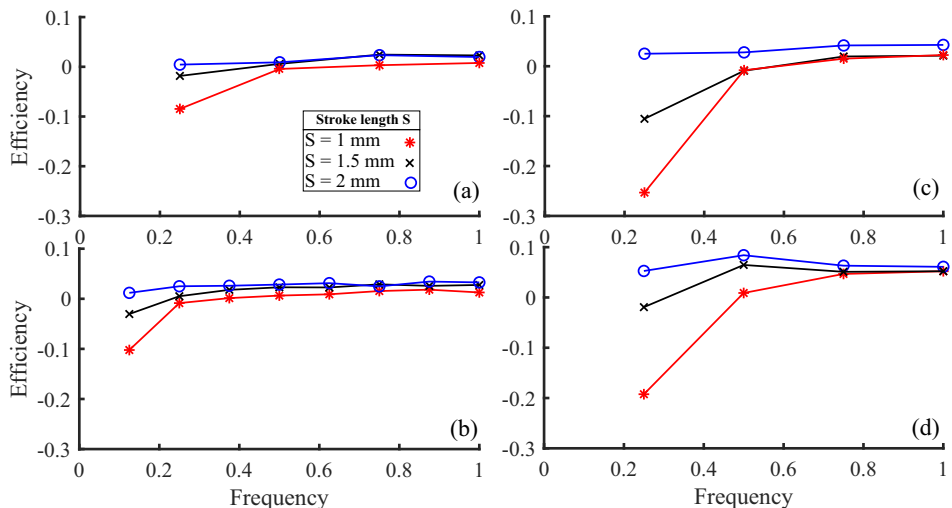


FIG. 4. Efficiency of flow rectification induced by the T-junction. $L_t = 80$ cm for all measurements shown, but γ varies: (a) $\gamma = 2$, (b) $\gamma = 4$, (c) $\gamma = 3$, and (d) $\gamma = 7$. The highest absolute efficiency occurs at the lowest frequencies, with diminishing efficiency observed at higher frequencies.

We then hypothesized that the deforming pressure relief membrane was effectively inducing peristalsis in the channel [25–27], producing the observed net flow. However, when we studied the motion of the membrane, we did not observe waves traveling along the length of the membrane, a requirement for net flux to be driven by peristalsis. Additionally, the membrane was mechanically constrained by surrounding walls and therefore could not accommodate peristaltic waves of sufficient amplitude to drive the observed flows, according to existing theory. To explain, we first estimate the actual deformation. In the most extreme case the syringe displaced 2.27 mL of fluid, while the channel had space to accommodate 2.50 mL. Assuming the most generous scenario where the membrane deflects uniformly (like a solid piston), the remaining space for a wave to travel would be $0.23 \text{ mL} / (8.26 \text{ mm} \times 95.2 \text{ mm}) = 0.29 \text{ mm}$. The minimum amplitude required to produce the measured net flow via peristaltic pumping can be calculated using the theory of Jaffrin and Shapiro [25], which is expressed in terms of the dimensionless flow rate $q_o = q / (A_t c_w)$, where q is the measured flow rate, A_t is the channel area, and c_w is the wave speed. From the net velocities shown in Fig. 3 we estimate $q = 10 \text{ mm}^3/\text{s}$ (tubing cross section 17.8 mm^2 and measured net velocities 0.6 mm/s). If we assume the wave travels the entire channel over a frequency of 0.5 Hz , the mid-range of our experiments, the wave speed is approximately $c_w = 50 \text{ mm/s}$. Combining these values with the cross-sectional area of the channel yields $q_o = 0.0076$. Jaffrin and Shapiro predict that the necessary nondimensional amplitude θ (percentage deformation of the channel size) is set by $q_o = 3\theta^2/2$ in a system with axially symmetric deformation, but since our apparatus has a deforming membrane on only one side, we would expect the required amplitude to be twice as large: $\theta = 14.25\%$, corresponding to 0.45 mm in dimensional terms. But the gap size is only 0.29 mm , so theory predicts that the observed flows could not be driven by peristalsis.

Furthermore, if large amplitude waves were driving flow, then the amplitude of those waves, and, in turn, the magnitude of the net induced flow, would depend on the stiffness of the tubing used. However, we did not observe the induced flow to vary with the tubing stiffness. Those observations ruled out peristalsis as a driving mechanism, suggesting that the major driver of mean flow was geometry-induced.

Flow rectification in looped flow geometries was recently presented by Nguyen and coworkers [14] using a similar experimental apparatus. They posited that the geometric features of their setup induced unique asymmetric vortex shedding phenomena at flow junctions that could be rectifying

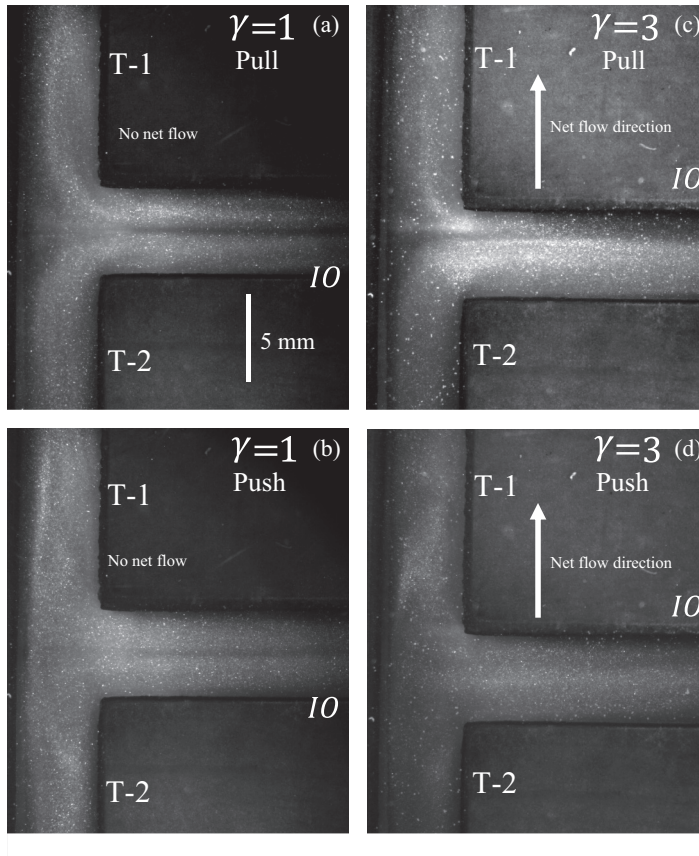


FIG. 5. Flow visualizations at the T-junction during the *push* and *pull* portions of a cycle. (a) $\gamma = 1$ configuration *pull* cycle, (b) $\gamma = 1$ configuration *push* cycle, (c) $\gamma = 3$ configuration *pull* cycle, (d) $\gamma = 3$ configuration *push* cycle. Dark regions near the centerline indicate flow separation, i.e., a separatrix. In the $\gamma = 1$ configuration, the separatrix is located in the center. In the $\gamma = 3$ configuration, it is shifted towards the inlet of T-1. Changing γ induces a time-dependent asymmetry in the flow, shown by the shifting of the separatrix position away from the center of the junction.

the oscillatory flows they imparted. Given the similarity of our experiments with those described by the authors, we visualized the flow features inside the T-junction to determine whether similar phenomena were driving net flow in our system.

B. Measurements at the T-junction

To observe the flow features forming at the T-junction, we first used rheoscopic fluid to qualitatively visualize the flow patterns. We divide our observations into two parts of the syringe's periodic cycle: the *push* phase, when the syringe injected fluid into the system, and the *pull* phase when the syringe removed fluid. Figure 5 shows snapshots of flow patterns at the T-junction during the *push-pull* phases for a single cycle across two configurations, $\gamma = 1$ and $\gamma = 3$. In each case, we observed the formation of a different separatrix—a region originating from IO where the flow bifurcated into two streams, ultimately leading to T-1 and T-2. In the $\gamma = 1$ case, we see that the separatrix is located in the middle of both the inlets to T-1 and T-2, during both the *push* and *pull* phases (Fig. 5). This suggests that equal amounts of fluid flowed into T-1 and T-2 during the push and pull phases of an oscillation, resulting in no net fluid transport. In the $\gamma = 3$ case, we observed

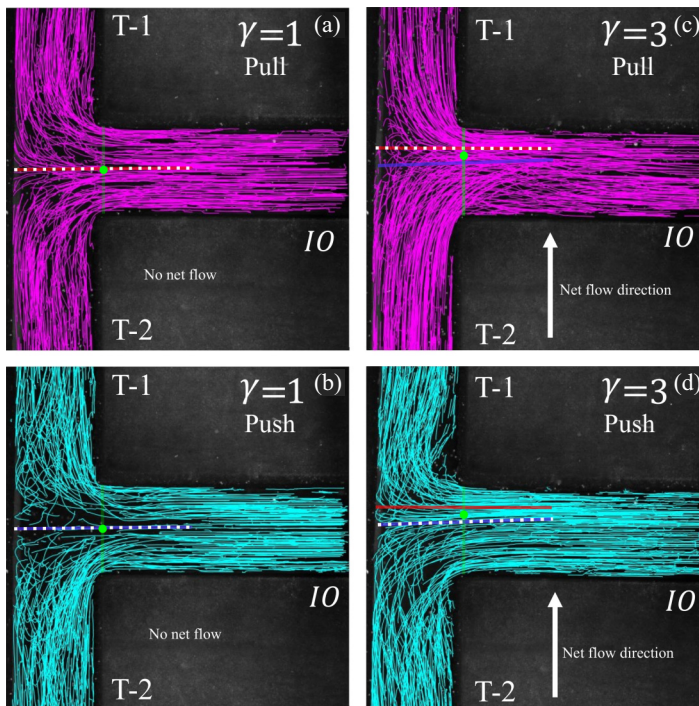


FIG. 6. Particle paths at the T-junction for two configurations at two different stages of the cycle. Magenta indicates paths occurring during the *pull* part of the cycle, whereas cyan indicates the *push* part. (a), (b) $\gamma = 1$; (c), (d) $\gamma = 3$. Blue (*push*) and red (*pull*) curves mark the separatrix location for each part of the cycle, determined from the measurements. Green dots indicate the separatrix location predicted by our analytic model (see Table I). The plots validate the observations from Fig. 5 where the separatrix shifted toward T-1 in the case of $\gamma = 3$ but not $\gamma = 1$. The case of $\gamma = 3$ [panels (c) and (d)] shows that the flow profiles differ during the *push* and *pull* portions of the cycle; the flow does not simply reverse. The separatrix indicates that the flow pathways differ depending on the cycle, which is not the case when $\gamma = 1$.

that the separatrix shifted towards the inlet for T-1 [Figs. 5(c) and 5(d)], suggesting more flow was directed towards T-2.

From our observations of the flow path, spatial differences between the *push* and *pull* cycles induced by the asymmetry when $\gamma > 1$ (as shown in Fig. 5) prompted us to further quantify the flow at the T-junction for the different configurations. We performed particle tracking measurements at the T-junction. Figure 6 shows particle path lines measured for the same conditions as those in Fig. 5. As shown in Fig. 6, the flow pathways significantly changed over each cycle due to the spatial asymmetry in the system. Particles favored displacement in a specific direction depending on the phase in an oscillation cycle. In experiments with particles, as in experiments with rheoscopic fluid, we determine the location of the separatrix by visual inspection.

C. Various orientations of the T-junction

The observations from Fig. 6 led us to inquire whether the geometric conditions produced at the T-junction were solely responsible for producing the observed directional flows. A simple way to vary geometric conditions significantly and test their impact was to change the orientation of the interconnections between the T-junction, the pressure relief membrane, and syringe pump.

Figure 7 shows the different configurations that we tested: *symmetric*, *short*, and *long*. In the *symmetric* configuration, the syringe pump was connected to the central arm of the T-junction with

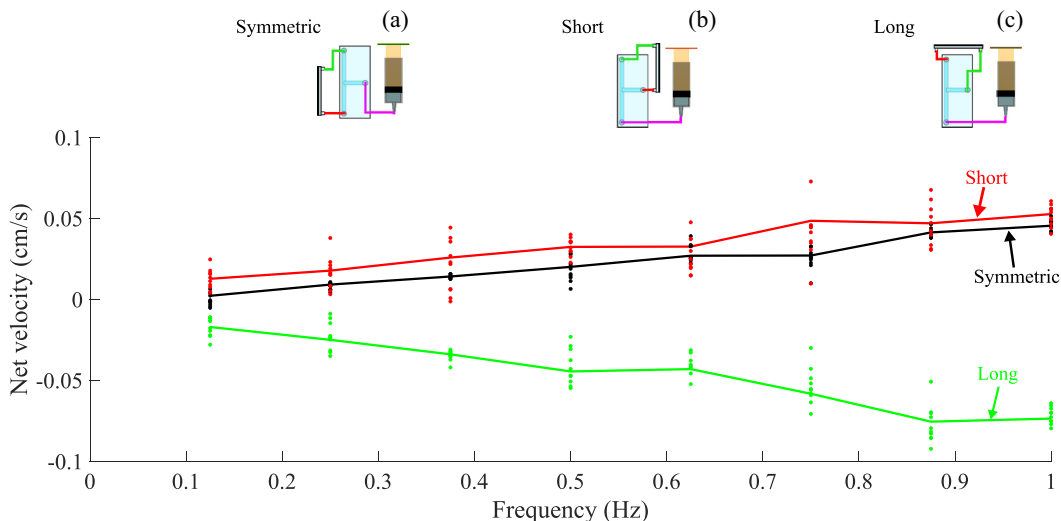


FIG. 7. Sketches of the configurations tested: (a) In the *symmetric* configuration, the central arm of the T is connected to the syringe pump (IO). (b) In the *short* configuration, the central arm is connected to the short tube (T-2). (c) In the *long* configuration, the central arm is connected to the long tube (T-1). The plot shows measurements of the net velocity in a section of T-1 for different interconnection configurations. For the *long* configuration, the direction of the flow is reversed. The effects of S and f on the magnitude of the net flow remained the same as shown in Fig. 3.

the two other arms connected to the inlet and outlet of the channel. In the *short* configuration, the central arm of the T-junction is connected to the short tube (T-2), and the other two arms are connected to the syringe pump and long tube (T-1). In the *long* configuration, the central arm is instead connected to the long tube (T-1). Also shown in the figure is the relationship between net velocity and f , which is similar in all three conditions, with the magnitude of the net velocity increasing with an increasing value of f . Measuring the net velocity at a section of T-1 for different configurations showed that the flow behavior was similar between the *symmetric* and *short* configurations, with net fluid flow in the counterclockwise direction. The magnitudes of flows induced in the *long* configuration were similar to those measured in the *short* configuration, but the flow direction was reversed: net flow was typically in the clockwise direction in the *long* configuration.

Figure 8 and the video provided as part of the Supplemental Material [28] show particle paths at the T-junction for the different configurations. Notably, one can observe a valving effect in the *long* configuration. The channel leading towards T-1 appears to behave as a sort of cavity during much of the flow period, where fluid prefers to follow the path between the syringe and T-2. This effect appears to be less intense during the *pull* phase compared with the *push* phase. The observed flow direction matches the measurements from Fig. 7.

D. Analytic prediction of separatrix location

We then devised a model to characterize the position of the separatrix using a simplified two-dimensional representation of the experimental apparatus, as shown in Fig. 9. The analytic model consisted of three channels connected to a T-junction. We considered steady flow in the analytic model, where the central channel is the inlet, while the other two channels are outlets. The boundary conditions included a flow rate Q_{in}^* imposed at the inlet and zero pressure imposed at the two outlets.

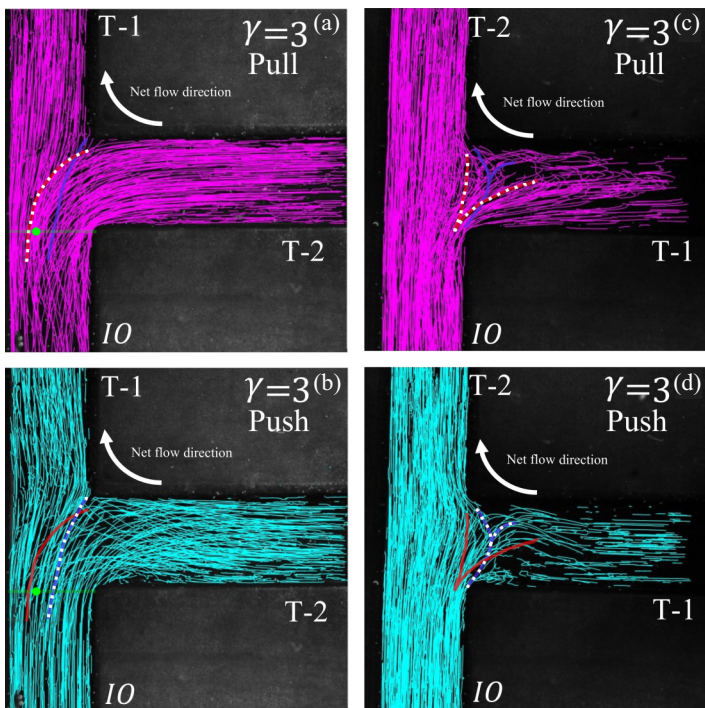


FIG. 8. Particle paths at the T-junction for the *short* and *long* configurations. Magenta indicates paths occurring during the *pull* phase of the cycle, whereas cyan indicates the *push* phase. (a), (b) *short* configuration; (c), (d) *long* configuration. Blue (*push*) and red (*pull*) curves mark the separatrix location for each part of the cycle, determined from the measurements. Green dots indicate the separatrix location predicted by our analytic model (see Table I). Over the cycle, different directions of flow are preferred, and as such a net velocity is induced in the loop. Note that the flow is reversed between configurations. In the *short* configuration particles move from T-2 to T-1 and *long* the direction is reversed.

To estimate whether the flow was laminar or turbulent for modeling purposes, we defined the Reynolds number as

$$Re = \frac{\max(u_{in})D_c}{\nu}, \quad (1)$$

where $\max(u_{in})$ is the maximum velocity at the inlet section, and D_c is the width of channel. The inlet velocity in the model is analogous to that of the syringe pump inlet IO. From our experiments, the highest Reynolds number was $Re = 1000$, so to first order we expect laminar dynamics similar to Poiseuille flow. For plane Poiseuille flow, the volume flow rate (per unit length in the third dimension) Q^* and channel length l are related by

$$Q^*l = \frac{\delta P D_c^3}{12\mu}, \quad (2)$$

where δP is the pressure difference between the channel's ends, μ is the dynamic viscosity of the fluid, and D_c is the channel width. In our model, Outlet-1 and Outlet-2 have the same width D_c and are subject to the same pressure drop δP because each connects the bifurcation to a place where the pressure is zero. Thus, the right-hand side of Eq. (2) is the same for both Outlet-1 and Outlet-2, and

$$\frac{Q_2^*}{Q_1^*} = \frac{l_1}{l_2} = \gamma, \quad (3)$$

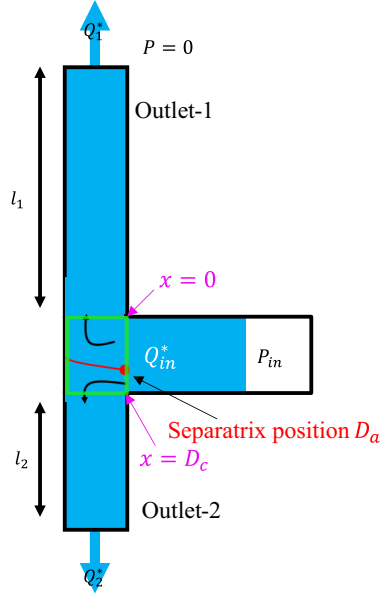


FIG. 9. Schematic of the analytic model. The model considers steady flow in a two-dimensional system of three channels connected by a T-junction. A flow rate is imposed in the central channel, simulating the conditions of the syringe pump. The two outlet channels (Outlet-1 and Outlet-2) have their own respective lengths and are open to the atmosphere. Each channel's flow rate is described by Q^* with its respective label. D_c is the width of the channel.

where subscripts correspond to Outlet-1 and Outlet-2. Note that reversing the flow—such that the fluid enters through the outlets and exits through the inlet—leaves this result unchanged.

Mass conservation at the bifurcation requires $Q_{in}^* = Q_1^* + Q_2^*$. Using Eq. (3) yields

$$Q_{in}^* = (\gamma + 1)Q_1^*. \quad (4)$$

By definition,

$$Q_{in}^* = \int_0^{D_c} u_{in} dx, \quad (5)$$

where

$$u_{in} = \frac{\delta P}{2\mu l} x(D_c - x)$$

is the fluid velocity for plane Poiseuille flow. If the separatrix is located at D_a , then the fluid filling the region $0 \leq x \leq D_a$ in the inlet channel ultimately passes to the Outlet-1 channel (see Fig. 9), and we can write

$$Q_1^* = \int_0^{D_a} u_{in} dx. \quad (6)$$

Combining Eqs. (4)–(6) and integrating leads to an expression for D_a :

$$\left(\frac{D_a}{D_c}\right)^3 - \frac{3}{2}\left(\frac{D_a}{D_c}\right)^2 + \frac{1}{2(\gamma + 1)} = 0. \quad (7)$$

TABLE I. Separatrix location D_a , expressed in terms of channel width D_c , for various values of the channel length ratio γ , as predicted by our analytic model.

γ	1	2	3	4	7
D_a/D_c	0.5	0.387	0.326	0.287	0.221

For a given value of γ , Eq. (7) has just one real root in the range $0 \leq D_a/D_c \leq 1$. Roots for the values of γ used in our experiments are shown in Table I and provide analytic predictions of the separatrix location in each case.

We validated our steady-state model numerically using ANSYS Fluent using the same configuration as in Fig. 9, choosing $D_c = 5$ mm. We performed steady-state simulations at $Re = 30$ to approximately match the values from the experimental measurements of the separatrix. For different values of γ , we observed that the separatrix shifted positions as shown by the stream function, plotted in Fig. 10. Additionally, the separatrix shifted positions between the *push* and *pull* phases. Comparing the analytic and numerical separatrix positions, we see that the analytic model predicts separatrix locations that vary with γ and are similar to those found in the steady-state simulations, as shown in Fig. 11. Notably, the analytic prediction of the separatrix position falls in between the two values that were numerically obtained for the *push* and *pull* cases. This shows that though the analytic model captures a major part of the flow dynamics, it fails to capture a systematic variation in the flow direction. (Recall that model predictions are independent of flow direction.) The remaining variation is likely due to nonlinear phenomena, such as flow separation, which affects the pressure field and in turn limits opposing flow. This separation effect cannot be captured by the model since it assumes (linear) Poiseuille flow. Flow separation is a nonlinear phenomenon. The effect on flow pathways is secondary in the sense that they affect the separatrix location less strongly than γ does (Fig. 11). However, since the linear behaviors captured by our simple model are entirely reversible with respect to the flow direction, those nonlinear phenomena are essential for providing rectification and therefore net flow.

We next used the simple model to estimate the position of the separatrix in experiments. The model produced accurate approximations for the $\gamma = 1$ configuration, as shown in Fig. 6. However, for the $\gamma = 3$ case, as with simulation results, predictions fell between the positions measured

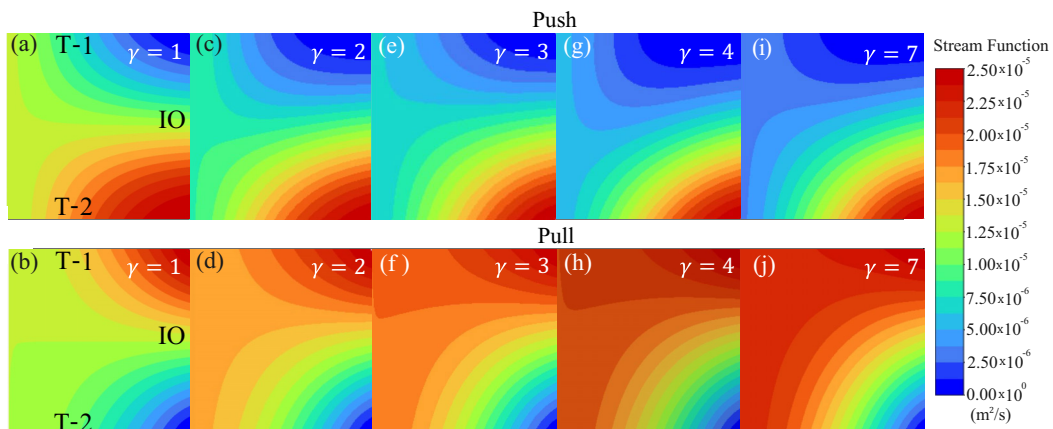


FIG. 10. Steady-state streamlines computed numerically for different values of γ for the model shown in Fig. 9, evaluated at $Re = 30$, for the region marked in green in Fig. 9. The dependency on the separatrix position on γ is clearly shown. As γ is increased the separatrix moves closer to T-1 (the top section of each plot).

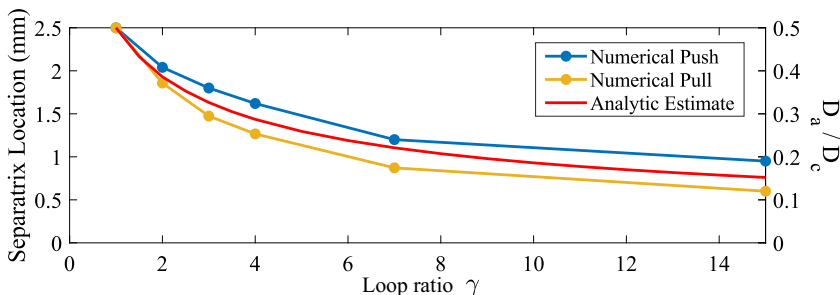


FIG. 11. Predictions of separatrix position from the analytical model and steady-state simulations for a channel of width $D_c = 5$ mm. The numerical values were calculated with flow states at $Re = 30$. The analytical values fall between the numerical values predicted for the *push* and *pull* phases. The analytic estimate provides a reasonable approximation of the separatrix position, as it falls between the two numerical cases. However, it is evident that the analytic estimate cannot fully capture the intricate dynamics of the flow in the T-junction, unlike the numerical results, which show a shift in the separatrix depending on the flow direction.

during the *pull* and *push* phases of the cycle, without matching either closely. During the *pull* phase, the separatrix position corresponded to a value of γ higher than the actual value, as if T-1 had been artificially lengthened, or equivalently, flow separation had decreased the flow rate into T-1. Conversely, during the *push* phase, the opposite occurred, suggesting that flow separation instead decreased the flow rate into T-2. Flow separation is visible in both the *push* and *pull* phases for the $\gamma = 3$ case, as seen in Fig. 6. Separation tends to occlude part of the channel, effectively reducing channel width and therefore affecting the flow rate at each of the channels T-1 and T-2. We propose that spatial asymmetry of the system induces nonlinear flow and generates a net flow. This nonlinear behavior was evinced by the time-dependent separatrix position, indicating that the flow pathways did not reverse perfectly between the *push* and *pull* cycles. Furthermore, simulation results in Fig. 12 demonstrate that as the Reynolds number tends towards zero, the analytic model predicts the separatrix position more accurately. On the other hand, as the Reynolds number increases and nonlinear effects become more important, the separatrix is shifted, a characteristic of the system exhibiting net flow.

IV. DISCUSSION AND CONCLUSIONS

In this study, we demonstrate that asymmetries arising from common flow pathway geometries such as T-junctions can rectify oscillatory flows and induce net directional transport. With

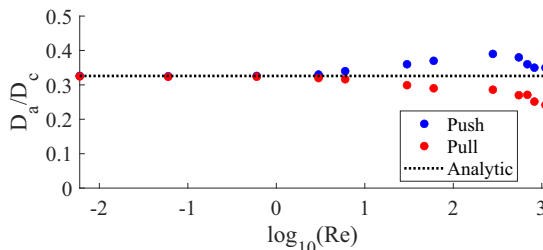


FIG. 12. Predictions of separatrix position from the analytical model and steady-state simulations for a channel width $D_c = 5$ mm. The numerical values were calculated with $\gamma = 3$. The analytical values fall between the numerical predictions for the *push* and *pull* phases at $Re > 1$. As the Reynolds number is decreased further, the position converges towards the analytically predicted value.

systematic experiments, we show that spatially asymmetric flow pathways result in asymmetric flow separation at the T-junction, such that reversing the motion of the syringe does not simply reverse the flow in the T-junction; rather, fluid is distributed differently during the *pull* phase than during the *push* phase. Rectification and a net flow therefore occur. We found that the magnitude of the induced flow increased monotonically with the frequency and amplitude of imposed oscillations. Additionally, we were able to change the direction of flow by choosing appropriate parameters even when the same geometric configuration in the flow loops was maintained as shown in the results in Fig. 3.

The concept of flow separation at a T-junction inducing a net flow is not exclusive to this study. Takagi *et al.* [29,30] and Propst [31] performed experimental and analytic analysis of fluid systems where two reservoirs were connected by a T-junction with an oscillating piston. The oscillatory motion of the piston induced an oscillating flow, which in turn was observed to produce a pressure gradient between reservoirs. Takagi *et al.* and Propst suggested that some nonlinear phenomenon is required in order to achieve a net pressure, but the scope of their studies was limited to measuring the net pressure and suggesting a potential mechanism inducing flow in the system. Our experimental measurements, numerical results, and analytic model together demonstrate that nonlinear flow dynamics in the system arise because of asymmetric flow pathways at the T-junction, as in the case of a symmetric geometry, we observe no net flow.

Nguyen *et al.* [14] observed a comparable phenomenon in a related system. They hypothesized that the net flow mechanism involved unstable flow due to flow separation and vortex shedding. Our observations from flow at the T-junction offer experimental and analytic validation of the hypothesis of Nguyen *et al.*. Their simulations showed separatrix behavior similar to what we saw in experiments. However, no potential mechanism was proposed or demonstrated to explain the phenomenon discussing the separatrix position. The experimental data we presented in Sec. III D validate the valving behavior they observed in numerical simulations in the flow at the T-junction. We identified the root cause of valving behavior with our simple analytic model, which indicated that the key component to the net flow is nonlinear dynamics in the flow pathway at the T-junction due to asymmetric flow separation over the flow oscillation cycles. Furthermore, we showed evidence and built on their conjecture that the direction of flow can also be controlled through simple manipulation of geometrical features of the setup, as covered in Sec. III C, which can be leveraged to achieve flow control in looped fluidic networks.

Our efficiency measurements align well with numerical predictions from Nguyen *et al.* They predicted that for the range of Womersley number [$Wo \approx 10$, where $Wo = (2\pi f l^2 / \nu)^{1/2}$], and an equivalent normalized amplitude of the particle displacement (0.5 to 2 tube inner diameters), the efficiencies are in the range of -0.1 to 0.1 . Those predictions are close to our measured efficiencies of -0.2 to 0.1 , as seen in Fig. 4. We experimentally demonstrated rectification in this parameter range, validating their numerical prediction and suggesting that geometric asymmetries could be exploited to achieve flow control.

The work we present has important limitations. Figure 7 shows that the orientation of the T-junction can affect the induced net flow. This sensitivity to the geometric conditions poses a limitation on the analytic and numerical results we presented given that we limited ourselves to a small set of geometries. In Fig. 12, we show that when $Re > 1$, the separatrix position deviates in simulations from the analytical predictions, although it matches closely for $Re < 1$. It is likely that for higher Reynolds numbers, as the flow becomes increasingly nonlinear, the sensitivity of the induced flow to geometric conditions will be more significant and our models may fail to capture accurate dynamics of the flow. The analytic model we presented does not consider any specific geometry where the channels bifurcate into two flows. The numerical and analytic modeling we performed was two dimensional. Since our analytic model presumed laminar Poiseuille flow, we expect its accuracy to diminish as the Reynolds number increases.

Our future work will focus on investigating lower Reynolds number flows in order to broaden the potential applications to biological systems with lower flow speeds, such as the glymphatic system, and other potential biological systems that exhibit puzzling valveless rectification, such as

the oscillatory flow of blood in an embryonic heart [32]. Preliminary observations in our apparatus and results from Ref. [8] suggest that this phenomenon can still be present at low flow velocities, as the geometric features of the channel have the potential to cause nonlinear phenomena, which are key to rectifying flow, even at low Reynolds numbers. Moreover, exploring more intricate loops with diverse junctions is a compelling subject for biophysical research. However, considering the broad implications of our findings, they can be extended to larger-scale fluid channel networks such as piped networks in hydraulic systems.

ACKNOWLEDGMENTS

This work was supported by the U.S. Army under award no. MURI W911NF1910280, by the U.S. National Center for Complementary and Integrative Health under Award No. R01AT012312, and by the BRAIN Initiative of the U.S. National Institutes of Health under Award No. U19NS128613.

R. Ibanez and A. Raghunandan contributed equally to this work.

-
- [1] Fluidic rectification, in *Encyclopedia of Microfluidics and Nanofluidics*, edited by D. Li (Springer US, Boston, 2008), p. 720.
 - [2] G. W. Schmid-Schönbein, The second valve system in lymphatics, *Lymphatic Res. Biol.* **1**, 25 (2003).
 - [3] M. H. Meissner, G. Moneta, K. Burnand, P. Gloviczki, J. M. Lohr, F. Lurie, M. A. Mattos, R. B. McLafferty, G. Mozes, R. B. Rutherford *et al.*, The hemodynamics and diagnosis of venous disease, *J. Vasc. Surg.* **46**, S4 (2007).
 - [4] K. Alitalo, The lymphatic vasculature in disease, *Nat. Med. (NY, US)* **17**, 1371 (2011).
 - [5] J. E. Moore, Jr and C. D. Bertram, Lymphatic system flows, *Annu. Rev. Fluid Mech.* **50**, 459 (2018).
 - [6] O. Forouzan, X. Yang, J. M. Sosa, J. M. Burns, and S. S. Shevkoplyas, Spontaneous oscillations of capillary blood flow in artificial microvascular networks, *Microvasc. Res.* **84**, 123 (2012).
 - [7] E. Katifori, G. J. Szöllösi, and M. O. Magnasco, Damage and fluctuations induce loops in optimal transport networks, *Phys. Rev. Lett.* **104**, 048704 (2010).
 - [8] Q. M. Nguyen, J. Abouezzi, and L. Ristroph, Early turbulence and pulsatile flows enhance diodicity of Tesla's macrofluidic valve, *Nat. Commun.* **12**, 2884 (2021).
 - [9] T. Nikola, Valvular conduit, US Patent No. 1,329,559, Washington, DC U.S. Patent and Trademark Office 1920.
 - [10] R. Tao, T. Ng, Y. Su, and Z. Li, A microfluidic rectifier for newtonian fluids using asymmetric converging-diverging microchannels, *Phys. Fluids* **32**, 052010 (2020).
 - [11] B. Thiria and J. Zhang, Ratcheting fluid with geometric anisotropy, *Appl. Phys. Lett.* **106**, 054106 (2015).
 - [12] A. Olsson, G. Stemme, and E. Stemme, A valve-less planar fluid pump with two pump chambers, *Sens. Actuators, A* **47**, 549 (1995).
 - [13] A. Groisman, M. Enzelberger, and S. R. Quake, Microfluidic memory and control devices, *Science* **300**, 955 (2003).
 - [14] Q. M. Nguyen, A. U. Oza, J. Abouezzi, G. Sun, S. Childress, C. Frederick, and L. Ristroph, Flow rectification in loopy network models of bird lungs, *Phys. Rev. Lett.* **126**, 114501 (2021).
 - [15] P. C. Sousa, F. T. Pinho, M. S. N. Oliveira, and M. A. Alves, Efficient microfluidic rectifiers for viscoelastic fluid flow, *J. Non-Newtonian Fluid Mech.* **165**, 652 (2010).
 - [16] J. J. Iliff, M. Wang, Y. Liao, B. A. Plogg, W. Peng, G. A. Gundersen, H. Benveniste, G. E. Vates, R. Deane, S. A. Goldman, E. A. Nagelhus, and M. Nedergaard, A paravascular pathway facilitates CSF flow through the brain parenchyma and the clearance of interstitial solutes, including amyloid β , *Sci. Transl. Med.* **4**, 147ra111 (2012).
 - [17] J. Tithof, K. A. Boster, P. A. Bork, M. Nedergaard, J. H. Thomas, and D. H. Kelley, A network model of glymphatic flow under different experimentally-motivated parametric scenarios, *iScience* **25**, 104258 (2022).

- [18] H. Mestre, J. Tithof, T. Du, W. Song, W. Peng, A. M. Sweeney, G. Olveda, J. H. Thomas, M. Nedergaard, and D. H. Kelley, Flow of cerebrospinal fluid is driven by arterial pulsations and is reduced in hypertension, *Nat. Commun.* **9**, 4878 (2018).
- [19] A. Raghunandan, A. Ladrón-de Guevara, J. Tithof, H. Mestre, T. Du, M. Nedergaard, J. H. Thomas, and D. H. Kelley, Bulk flow of cerebrospinal fluid observed in periarterial spaces is not an artifact of injection, *eLife* **10**, e65958 (2021).
- [20] A. Ladrón-de-Guevara, J. K. Shang, M. Nedergaard, and D. H. Kelley, Perivascular pumping in the mouse brain: Improved boundary conditions reconcile theory, simulation, and experiment, *J. Theor. Biol.* **542**, 111103 (2022).
- [21] D. Borrero-Echeverry, C. J. Crowley, and T. P. Riddick, Rheoscopic fluids in a post-Kalliroscope world, *Phys. Fluids* **30**, 087103 (2018).
- [22] D. H. Kelley and N. T. Ouellette, Using particle tracking to measure flow instabilities in an undergraduate laboratory experiment, *Am. J. Phys.* **79**, 267 (2011).
- [23] A. I. Hickerson, D. Rinderknecht, and M. Gharib, Experimental study of the behavior of a valveless impedance pump, *Exp. Fluids* **38**, 534 (2005).
- [24] V. Zislin and M. Rosenfeld, Impedance pumping and resonance in a multi-vessel system, *Bioengineering* **5**, 63 (2018).
- [25] M. Y. Jaffrin and A. H. Shapiro, Peristaltic pumping, *Annu. Rev. Fluid Mech.* **3**, 13 (1971).
- [26] A. H. Shapiro, M. Y. Jaffrin, and S. L. Weinberg, Peristaltic pumping with long wavelengths at low Reynolds number, *J. Fluid Mech.* **37**, 799 (1969).
- [27] S. L. Weinberg, E. C. Eckstein, and A. H. Shapiro, An experimental study of peristaltic pumping, *J. Fluid Mech.* **49**, 461 (1971).
- [28] See Supplemental Material at <http://link.aps.org/supplemental/10.1103/PhysRevFluids.8.113101> for SupplementalLong and SupplementalShort movies of the experimental data are shown in Fig. 8. The supplemental material movies labeled long and short match the configurations long and short shown in Fig. 8.
- [29] S. Takagi and T. Saijo, Study of a piston pump without valves: 1st report, on a pipe-capacity-system with a T-junction, *Bull. JSME* **26**, 1366 (1983).
- [30] S. Takagi and K. Takahashi, Study of a piston pump without valves: 2nd report, pumping effect and resonance in a pipe-capacity-system with a T-junction, *Bull. JSME* **28**, 831 (1985).
- [31] G. Propst, Pumping effects in models of periodically forced flow configurations, *Phys. D (Amsterdam, Neth.)* **217**, 193 (2006).
- [32] N. Sarvazyan, Building valveless impedance pumps from biological components: Progress and challenges, *Front. Physiol.* **12**, 770906 (2022).